A&A 613, A32 (2018)
https://doi.org/10.1051/0004-6361/201732183

Astronomy & Astrophysics

Empirical models of Jupiter's interior from *Juno* data

Moment of inertia and tidal Love number k_2

Dongdong Ni[1,2]

[1] Space Science Institute, Macau University of Science and Technology, Macao, PR China
e-mail: ddni@must.edu.mo
[2] Institute for Planets and Exoplanets, University of California, Los Angeles, CA 90095-1567, USA

Received 27 October 2017 / Accepted 28 February 2018

ABSTRACT

Context. The *Juno* spacecraft has significantly improved the accuracy of gravitational harmonic coefficients J_4, J_6 and J_8 during its first two perijoves. However, there are still differences in the interior model predictions of core mass and envelope metallicity because of the uncertainties in the hydrogen-helium equations of state. New theoretical approaches or observational data are hence required in order to further constrain the interior models of Jupiter. A well constrained interior model of Jupiter is helpful for understanding not only the dynamic flows in the interior, but also the formation history of giant planets.
Aims. We present the radial density profiles of Jupiter fitted to the *Juno* gravity field observations. Also, we aim to investigate our ability to constrain the core properties of Jupiter using its moment of inertia and tidal Love number k_2 which could be accessible by the *Juno* spacecraft.
Methods. In this work, the radial density profile was constrained by the *Juno* gravity field data within the empirical two-layer model in which the equations of state are not needed as an input model parameter. Different two-layer models are constructed in terms of core properties. The dependence of the calculated moment of inertia and tidal Love number k_2 on the core properties was investigated in order to discern their abilities to further constrain the internal structure of Jupiter.
Results. The calculated normalized moment of inertia (NMOI) ranges from 0.2749 to 0.2762, in reasonable agreement with the other predictions. There is a good correlation between the NMOI value and the core properties including masses and radii. Therefore, measurements of NMOI by *Juno* can be used to constrain both the core mass and size of Jupiter's two-layer interior models. For the tidal Love number k_2, the degeneracy of k_2 is found and analyzed within the two-layer interior model. In spite of this, measurements of k_2 can still be used to further constrain the core mass and size of Jupiter's two-layer interior models.

Key words. methods: numerical – planets and satellites: general – planets and satellites: individual: Jupiter – planets and satellites: interiors

1. Introduction

The *Juno* spacecraft acquired science observations of Jupiter on 27 August 2016 and since then has measured Jupiter's gravitational field to high precision during its first two perijoves. The accuracy of the gravitational harmonic coefficients J_4, J_6 and J_8 has been improved by more than a factor of five compared with the previous values detected by Pioneer 10 and 11 and by Voyager 1 and 2 (Folkner et al. 2017; Bolton et al. 2017). This provides excellent observational constraints on interior models of Jupiter. Although significant progress has been made in detecting Jupiter's gravity field with the development of detection equipment and technology, there are still uncertainties in interior models such as hydrogen-helium equation of state (EOS) and hydrogen-helium phase separation (Kong et al. 2016; Miguel et al. 2016; Hubbard & Militzer 2016). The EOS of hydrogen has been widely investigated for many decades owing to its important applications. Recent laboratory measurements on fluid deuterium have been able to reach the megabar pressure range but various results have been achieved at pressures above 1 Mbar (Fortney & Nettelmann 2010; Guillot 1999, 2005; McMahon et al. 2012; Militzer et al. 2016). Moreover, laboratory temperatures are typically much hotter than the Jupiter adiabat for the pressure of interest. So one has to resort to theoretical calculations of thermodynamically consistent EOS over the entire domain of pressure and temperature spanned by Jupiter's interior. There are various EOSs available based on different methods and considerations. For example, Saumon et al. (1995) presented new EOSs for hydrogen and helium using the free-energy minimization method within the chemical picture, namely SCvH. Later Saumon & Guillot (2004) used the currently available hydrogen or deuterium EOSs to probe the internal structures of Jupiter and Saturn. The mass predictions of cores and heavy elements were found to depend upon the hydrogen EOS. Along with the progress in computer capacity and numerical techniques, EOSs have also been calculated from ab initio simulations within the physical picture since 2006 (Nettelmann et al. 2008, 2012; Becker et al. 2014; Militzer et al. 2008; Militzer & Hubbard 2013). Recently Miguel et al. (2016) have investigated the effect of different EOSs including ab initio EOSs on Jupiter's internal structure, where the conclusions of Saumon & Guillot (2004) were confirmed and the differences in the interior models of Jupiter were discussed. Considering the uncertainties of EOS and its effect on Jovian interiors, Anderson & Schubert (2007) proposed an alternative viewpoint to investigate Saturn's internal structure. They adopted a six-degree polynomial to describe the radial density profile in Saturn and constrained the polynomial coefficients using the

data on Saturn's shape and gravity field; the internal pressure profile was then obtained from the hydrostatic equations and the pressure-density relation was inferred as EOS. This model is consistent with the available detecting data and well interprets the key features of Saturn's interior. It is a useful approximation to more complicated models that require EOS as an input model parameter.

In this work, we intend to use the *Juno* data to constrain interior models of Jupiter, based on the viewpoint of Anderson & Schubert (2007). The six-degree polynomial interior model of Anderson & Schubert (2007); Helled et al. (2009) is generalized from one-layer to two-layer frameworks. Different two-layer models are constructed in terms of various core properties and the corresponding density profile is constrained by the *Juno* data. From the viewpoint of giant planet formation theories, one must have some knowledge of the interior structure and composition of Jupiter, which are of great importance to test formation models. The core mass of $\sim$10 $M_\oplus$ (Earth masses) in Jupiter would provide an observational support for the core accretion model (Helled 2012) and hence great effort has been devoted to better constrain Jupiter's core mass. Here possible observational constraints on the core properties of Jupiter are discussed, in addition to gravitational coefficients. One constraint is a measurement of Jupiter's moment of inertia. The ongoing *Juno* mission could measure Jupiter's moment of inertia thanks to precise measurements of the spacecraft's acceleration and long service lifetimes of 20 months. Helled et al. (2011) performed an error analysis of *Juno* measurements, yielding a standard error of about 0.2%. The other potential constraint is a measurement of Jupiter's tidal Love number k_2, since it is sensitive to the level of central condensation of a planet. The tidal Love number k_2 has been widely used to constrain the interior models of exoplanets whose gravitational moment measurements are inaccessible (Kramm et al. 2011, 2012). As for the Jovian planets, the first determination of Saturn's Love number was achieved recently from *Cassini* astrometric data by Lainey et al. (2017). In common with the Saturnian system, tidal effects among the Jovian system could be derived from *Juno* astrometric observations of the satellites over an extended time period. Alternatively, k_2 could be directly determined from the *Juno* gravity science measurements as one main objective of the *Juno* mission is to estimate Jupiter's gravity field.

To address this issue, we first present the empirical two-layer model and introduce the calculation of moments of inertia and tidal Love numbers in Sect. 2. Various two-layer planetary models are also constructed in terms of core properties. Then, in Sect. 3, we discuss the practical aspects of our calculations and present the detailed results of our calculations. The dependence of our results on the core properties is analyzed in detail, together with the ability to constrain the internal structure of Jupiter. Finally, the main results of this paper are summarized in Sect. 4.

2. Theoretical framework

2.1. Empirical interior model

The six-degree polynomial interior model of Anderson & Schubert (2007); Helled et al. (2009) was originally developed for Saturn's interior, where the mean radius s internal to the planet is used so that the internal structure can be described by the single variable. In view of the rotational flattening of giant planets, one might think a general three-dimensional integral description is required in modeling giant planets. However, this problem can be properly handled, as reviewed by Zharkov & Trubitsyn (1978); Guillot (1999). One can express the radius r with the mean radius s as well as Legendre polynomials P_n and introduce a rotation term into hydrostatic equations. This procedure is sufficient to take into account the rotation influences. So the traditional equations of stellar structure in one dimension (spherically symmetric) can be used for giant planets, where the mean radius s is used as the independent variable rather than r. The internal structure of giant planets is governed by the hydrostatic and mass-continuity equations:

$$\rho(s)^{-1}\mathrm{d}P(s)/\mathrm{d}s = -g(s) + 2\omega^2 s/3, \tag{1}$$

and

$$\mathrm{d}m(s)/\mathrm{d}s = 4\pi s^2\rho(s), \tag{2}$$

where $P(s)$ is the pressure at mean radius s, $\rho(s)$ is the density at mean radius s, $g(s) = Gm(s)/s^2$ is the gravity at mean radius s[$m(s)$ is the mass enclosed within mean radius s], and ω is the planet's angular velocity. One introduces dimensionless planetary units of mean radius, density, mass, and pressure, such that $s = xR_p$, $\rho(s) = \eta(x)(3M/4\pi R_p^3)$, $m(s) = \alpha(x)M$, $P(s) = \xi(x)(3GM^2/4\pi R_p^4)$ (M is the planet's total mass and R_p is planet's mean radius). The two equations above are transformed to

$$\eta(x)^{-1}\mathrm{d}\xi(x)/\mathrm{d}x = -\alpha(x)/x^2 + 2q_{\mathrm{rot}}x/3, \tag{3}$$

and

$$\mathrm{d}\alpha(x)/\mathrm{d}x = 3x^2\eta(x), \tag{4}$$

where q_{rot} is a smallness parameter representing the ratio between centrifugal and gravitational forces, $q_{\mathrm{rot}} = \omega^2 R_p^3/GM$. In the work of Anderson & Schubert (2007), the density distribution $\eta(x)$ is represented by a six-degree polynomial as a function of the normalized mean radius x,

$$\eta(x) = a_0 + a_2x^2 + a_3x^3 + a_4x^4 + a_5x^5 + a_6x^6\,. \tag{5}$$

We note that the first-degree term is set to zero so that the derivative of the density goes to zero at the center $x = 0$. Then, three boundary conditions are imposed: $\eta(x)$ and its first derivative are both zero at $x = 1$ and $\alpha(x)$ is equal to one at $x = 1$. One can obtain the following equations:

$$a_0 + a_2 + a_3 + a_4 + a_5 + a_6 = 0, \tag{6}$$

$$2a_2 + 3a_3 + 4a_4 + 5a_5 + 6a_6 = 0, \tag{7}$$

$$a_0 + 3a_2/5 + a_3/2 + 3a_4/7 + 3a_5/8 + a_6/3 = 1. \tag{8}$$

There are three degrees of freedom in the polynomial and the available data on Saturn's gravitational field (J_2, J_4, and J_6) are used to determine them by the nonlinear least squares fitting. Once the density profile is given, the profiles of the internal pressure and mass are known by solving Eqs. (3) and (4). This model well accounted for the key feature of Saturn's interior and wrapped uncertainties and assumptions into some adjustable parameters in the density distribution. It serves as a good approximation to complex interior models in which uncertainties concerning equations of states and hydrogen-helium demixing are involved.

But the six-degree polynomial interior model ignores density discontinuities at the surface of dense cores. Here it is generalized from one-layer to two-layer models, consisting of a core with constant density a_C and an envelope with five-degree

polynomial density. The fractional internal density of Jupiter is expressed as

$$\begin{aligned} \eta_E(x) &= a_0 + a_1 x + a_2 x^2 + a_3 x^3 + a_4 x^4 + a_5 x^5 , \quad x_C \le x \le 1 , \\ \eta_C(x) &= a_C , \qquad\qquad\qquad\qquad\qquad\quad 0 \le x \le x_C . \end{aligned} \tag{9}$$

The functions $\eta_E(x)$ and $\eta_C(x)$ are, respectively, the fractional internal densities of the envelope and core, and the core density $\eta_C(x)$ is always larger than $\eta_E(x)$. The quantity x_C denotes the radius of the central core in planet radii and the ratio of core mass to total mass is given by $m_C = a_C x_C^3$. As before, there are three constraints on the polynomial coefficients. The first is $\eta_E(x) = 0$ at the surface $x = 1$, suggesting $a_0 + a_1 + a_2 + a_3 + a_4 + a_5 = 0$. The second is $\mathrm{d}\eta_E(x)/\mathrm{d}x = 0$ at the surface $x = 1$. That is, one obtains $a_1 + 2a_2 + 3a_3 + 4a_4 + 5a_5 = 0$. The third requires that the total mass must equal to Jupiter's mass,

$$\begin{aligned} a_0(1 - x_C^3) + 3a_1(1 - x_C^4)/4 + 3a_2(1 - x_C^5)/5 + a_3(1 - x_C^6)/2 \\ +3a_4(1 - x_C^7)/7 + 3a_5(1 - x_C^8)/8 + m_C = 1. \end{aligned} \tag{10}$$

First, we constructed different two-layer models in terms of core properties such as models either with constant core mass, or with constant core size, or with constant core density, as well as extreme cases of $\eta_C(x_C) = \eta_E(x_C)$. Next, in combination with the above three constraints, the six polynomial coefficients a_n were determined by a nonlinear least squares fit to the available data on Jupiter's shape and gravity field. The gravitational zonal harmonic coefficients are weighted integrals over the internal density distribution $\rho(r, \theta)$,

$$J_{2i} = -\frac{1}{MR_{\mathrm{eq}}^{2i}} \int_V r^{2i} P_n(\cos\theta)\rho(r,\theta) d^3 r, \tag{11}$$

where θ is the latitude. In practice, a reasonable guess of $\eta_E(x)$ is provided, even zonal harmonics J_{2i} are calculated in terms of the theory of figures (Zharkov & Trubitsyn 1975, 1978), and the difference between the calculated harmonics and the observed ones are then used to correct the polynomial coefficients. This procedure is iteratively implemented for good convergence. *Juno*'s observations (J_2, J_4, J_6, J_8, and R_{eq}) are used in the fitting process and they are given in Table 1.

Following the theory of figures (Zharkov & Trubitsyn 1975, 1978), the level surfaces are given by the figure functions $s_{2i}(s)$ in the form

$$r(s,\theta) = s\left[1 + \sum_{i=0}^{\infty} s_{2i}(s) P_{2i}(\cos\theta)\right]. \tag{12}$$

By definition, the total potential is independent upon the latitude θ at a fixed mean radius s. In this manner, any dependence on (r, θ) is replaced by dependence on (s, θ) and the theory of order n can be achieved by truncation of the expansion (12) for $i \le n$. The even zonal harmonics J_{2i} are then evaluated as $J_{2i} = (-R_p/R_{\mathrm{eq}})^{2i} S_{2i}(1)$. The functions $S_{2i}(x)$ are the integrals of the form

$$S_{2i}(x) = \frac{1}{x^{2i+3}} \int_0^x \mathrm{d}x' \frac{\rho(x')}{\bar{\rho}} \frac{\mathrm{d}}{\mathrm{d}x'}[x'^{2i+3} f_{2i}(x')], \tag{13}$$

where $\bar{\rho}$ is the mean density and f_{2i} are nonlinear functions of the variables x', $s_0(x')$, ..., $s_{2n}(x')$. The detailed results for $f_{2i}(x)$ and $S_{2i}(x)$ can be found in Zharkov & Trubitsyn (1975, 1978). Here the fifth-order theory of figures is used for the calculations of Jupiter's shape and gravity field.

Table 1. Jupiter's shape and gravity-field data.

Parameter	Jupiter	Reference
GM (km^3 s^{-2})	126686533.0 ± 2.0	(1)
$J_2 \times 10^6$	14696.514 ± 0.272	(1)
$J_4 \times 10^6$	−586.623 ± 0.363	(1)
$J_6 \times 10^6$	34.244 ± 0.236	(1)
$J_8 \times 10^6$	−2.502 ± 0.311	(1)
R_{eq} (km)	71492 ± 4	(2)
R_{polar} (km)	69911 ± 6	(2)
P_ω (s)	35729.7 ± 4.1	(3)

References. (1) Folkner et al. (2017); (2) Seidelmann et al. (2007); (3) Guillot (2005)

2.2. Moment of inertia

There is another important quantity associated with the internal density structure of a planet, namely moment of inertia C, or its normalized form $C_N = C/MR_p^2$. So one can use it to further constrain the two-layer interior models of Jupiter. With respect to terrestrial planets such as Mars and Earth, it is more difficult to measure moments of inertia for the giant planets. The possible determination of Jupiter's moment of inertia from *Juno* spacecraft was discussed by Helled et al. (2011) and a standard error of measured normalized moments of inertia (NMOI) was estimated as about 0.2%. Besides, we would like to note that Jupiter's NMOI today might be different from its primordial one since Jupiter's internal structure evolves over time. Helled (2012) investigated the evolution of Jupiter's NMOI assuming that Jupiter undergoes core erosion. In this work, we have only concentrated on Jupiter's current NMOI.

Theoretically, one usually uses the Radau–Darwin relation to estimate NMOI values. It gives the first-order response of a planet to rotational distortion,

$$C_N = \frac{2}{3}\left[1 - \frac{2}{5}\left(\frac{5}{3\Lambda_{2,0} + 1} - 1\right)^{1/2}\right], \tag{14}$$

with $\Lambda_{2,0} = J_2/q_{\mathrm{rot}}$. Using *Juno*'s gravitational observations, the Radau–Darwin relation suggests Jupiter's NMOI of about 0.2649. Actually, the moment of inertia of a planet is in principle calculated from its internal density distribution. Based on the above empirical two-layer model, the NMOI is related to the density distribution as follows,

$$C_N = 2\left(\int_0^{x_C} \eta_C(x) x^4 \, \mathrm{d}x + \int_{x_C}^1 \eta_E(x) x^4 \, \mathrm{d}x\right), \tag{15}$$

where Jupiter's shape deformation is not included. Considering a large degree of rotational flattening for Jupiter, it is of interest to take into account the shape of the internal density distribution. This can be achieved in terms of the theory of figures (Zharkov & Trubitsyn 1975, 1978), where the level surfaces are given by the figure functions $s_{2i}(s)$ [see Eq. (12)]. By abbreviating the level surface as $r = s(1 + \sum)$, the NMOI is written as

$$C_N = \frac{\int_{-1}^1 \mathrm{d}\cos\theta(1 - \cos^2\theta) \int_0^1 \mathrm{d}x(\mathrm{d}r/\mathrm{d}s) x^4 (1 + \sum)^4 \eta(x)}{\int_{-1}^1 \mathrm{d}\cos\theta \int_0^1 \mathrm{d}x(\mathrm{d}r/\mathrm{d}s) x^2 (1 + \sum)^2 \eta(x)}. \tag{16}$$

Once the density distribution is determined from the data on Jupiter's shape and gravity field, the corresponding NMOI is

calculated from Eq. (16). We were able to construct different two-layer models by varying the core properties and then investigate the variation of NMOI. We note that the NMOI expressions (15) and (16) are given under the assumption that Jupiter executes rigid-body rotation or differential rotation only appears in the atmosphere of Jupiter.

2.3. Tidal Love number k_2

The tidal Love number k_2 will tell us about the level of central condensation of a planet independently of even zonal harmonics J_{2n} and moments of inertia. Very recently Saturn's second-degree Love number k_2 has been determined from the *Cassini* astrometric data by Lainey et al. (2017). The tidal distortion of Jupiter arising from the Galilean moons has, however, not yet been detected since the largest influence of tides on Jupiter's gravitational coefficient J_2 is only on the order of magnitude of 10^{-7}, even smaller than the measured $J_6 \sim 10^{-5}$ (Gavrilov et al. 1975). The ongoing *Juno* spacecraft exhibits an unprecedented precision, approaching a relative precision of 10^{-9} (Kaspi et al. 2010). So Jupiter's second-degree tidal distortion to its nearest large moon (Io) is expected to be detected in the gravity field (Wahl et al. 2016). One can use k_2, like moments of inertia, to further constrain the two-layer interior models of Jupiter.

The tidal-rasing potential from an external perturbing body of mass m moving in a circular orbit of radius a around a planet with mass M and mean radius R_p is expressed as

$$W(s) = \sum_{n=2}^{\infty} W_n(s) = (Gm/a) \sum_{n=2}^{\infty} (s/a)^n P_n(z). \tag{17}$$

where s is the radial coordinate of the considered point on the planet, and z is the angle between the radius vector of the considered point at s and the direction to the center of mass of the perturbing body at a. Correspondingly, the perturbation of the planet's potential is given by $V_n^{\rm in}(s) = K_n(s) W_n(s)$, where $K_n(s)$ is the Love function and $k_n \equiv K_n(R_p)$ are the dimensionless Love numbers. According to the treatment of Gavrilov et al. (1975); Gavrilov & Zharkov (1977), the function $T_n(s)$ determining the total change of the planet's potential is introduced and the Love numbers k_n are dependent upon $T_n(s)$ as follows,

$$k_n = \frac{T_n(R_p)}{R_p g_0} - 1, \tag{18}$$

where g_0 is the surface gravity acceleration for the unperturbed planet and $T_n(R_p)$ denotes the value of the function $T_n(s)$ at the planet's surface $s = R_p$. To determine the Love numbers k_n, it is necessary to achieve the function $T_n(s)$, which satisfies the second-order differential equation (Gavrilov et al. 1975; Gavrilov & Zharkov 1977)

$$T_n''(s) + \frac{2}{s} T_n'(s) + \left[\frac{4\pi G \rho'(s)}{V'(s)} - \frac{n(n+1)}{s^2} \right] T_n(s) = 0. \tag{19}$$

In Eq. (19), the prime denotes the radial derivative with respect to s, and $\rho(s)$ and $V(s)$ are, respectively, the unperturbed density distribution and gravitational potential of the planet. The differential equation (19) is solved with boundary conditions. First, the function $T_n(s)$ is regular at the origin, $T_n(0) = 0$. Second, on the planet's surface $s \to R_p$ the function $T_n(s)$ satisfies the condition $T'(s) = -(n+1)T(s)/R_p + (2n+1)g_0$. In two-layer or three-layer models, there are generally density discontinuities such as $s = x_C R_p$. At these points the function $T_n(s)$ should satisfy the jump conditions (Gavrilov et al. 1975; Gavrilov & Zharkov 1977):

$$T_n(x_C^+) = T_n(x_C^-), \tag{20}$$

$$T_n'(x_C^+) - T_n'(x_C^-) = \frac{4\pi G}{V'(x_C)} \left[\rho(x_C^-) - \rho(x_C^+) \right] T_n(x_C), \tag{21}$$

where the plus (negative) sign stands for a position just outside (inside) the discontinuity. Once the density distribution is determined from the data on Jupiter's shape and gravity field, the differential Eq. (19) is numerically solved for the Love numbers. And furthermore, the dependence of k_2 on the core properties is investigated within the two-layer model.

Recently Wahl et al. (2016, 2017a) introduced the non-perturbative concentric Maclaurin spheroid (CMS) method to calculate the static tidal response of Jupiter and Saturn and the enhancement of k_2 was found with respect to the method of Gavrilov et al. (1975) presented above. This is understood as the contributions from terms which are on the order of the product of the tidal and rotational perturbations, while the method of Gavrilov et al. (1975) did not take into account these terms. In spite of some differences between the absolute k_2 values yielded from the method of Gavrilov et al. (1975) and from the non-perturbative CMS method, the systematic variation of k_2 with the core properties is expected to remain almost the same for these two methods.

3. Model results

To tell our story, we imposed the following assumptions on our empirical two-layer model: (1) The mass of the dense central core is not larger than 40 $M_\oplus$. That is, $m_C \leq 0.12585$. (2) The central core is made of an unknown combination of refractory material ("rocks" with typical density of about 20 g cm^{-3}) and more volatile species ("ices" with typical density of about 10 g cm^{-3}). For comprehensiveness, the core density is assumed to be not larger than 30 g cm^{-3} (Helled et al. 2011). (3) The density $\eta(x)$ monotonically varies with the radius x, showing $\mathrm{d}\eta(x)/\mathrm{d}x \leq 0$ at any points internal to the planet. We pay special attention to the core-envelope boundary (CEB) x_C where the density jump $\Delta\eta_{CEB} = \eta_C(x_C) - \eta_E(x_C)$ cannot be negative (the extreme case is $\Delta\eta_{CEB} = 0$). These assumptions are based on our current knowledge of Jupiter (Guillot 2005; Fortney & Nettelmann 2010; Militzer et al. 2016). With these in mind, we constructed different two-layer models in terms of core properties, such as models with constant core mass fraction $m_C \leq 0.12585$, models with constant core density $\rho_C \leq 30$ g cm^{-3}, and extreme cases of $\Delta\eta_{CEB} = 0$. The radial density profile is then determined within these two-layer models in terms of the data on Jupiter's shape and gravity field as shown in Table 1. In general, the gravitational harmonic coefficients J_2 and J_4 are well reproduced within the measurement uncertainties, together with the equatorial radius R_e. The agreement between the calculated values of J_6 and J_8 and the *Juno* data is slightly worse as compared with the case of J_2 and J_4, but it is still acceptable. To gain insight into this, Table 2 summarizes the results for some representative two-layer models. We note that the observed data shown in Table 1 are also listed for comparison. In the empirical two-layer model, the density profile $\eta(x)$ is required to monotonically decrease with increasing the radius x in the envelope and furthermore exhibit denser cores $\Delta\eta_{CEB} \geq 0$. Figure 1 illustrates the density profiles for two representative models with the core mass fraction $m_C = 0.020$: the maximum core density of $\rho_C = 30$ g cm^{-3} (solid black lines) and the zero density jump at

the CEB $\Delta\eta_{CEB} = 0$ (blue dashed lines). We note that the density values were normalized by a constant density of $\rho_{\rm pu} = M/R_p^3 = 5.555$ g cm^{-3} in the figure. For these two cases, the resulting core size fractions are, respectively, $x_C = 0.096$ and $x_C = 0.142$. And their difference is obvious in the core region owing to the different core properties adopted in the two-layer models and then becomes reduced with increasing the radius since both of them are well constrained by the available data. Moreover, the density structure from the three-layer model of Guillot (1999); denoted by Jup-Ad-PPT is also shown for comparison, where the dense core is characterized by $m_C = 0.020$ and $x_C = 0.126$. Indeed, the core size fraction of Jup-Ad-PPT is located between our two cases with the same core mass fraction. In the envelope, the density distribution of our two cases exhibits a smaller variation rate in the region of $x = 0.50$–0.70 beneath the helium-demixing zone and then a larger variation rate in the region of $x = 0.13$–0.30 above the core. This difference is more significant than what one would find in the interior models using different EOS. Jupiter's barotrope for pressure ≤1 Mbar lies on the Galileo probe adiabat but at higher pressures follows a higher-entropy adiabat owing to hydrogen-helium immiscibility (Hubbard & Militzer 2016). Furthermore, the dilute core model of Wahl et al. (2017b) suggests that heavy elements are dissolved in hydrogen-helium mixture and expanded outward through a portion of Jupiter. This would bring in not only the higher density above the core but also an enhancement of the entropy in the metallic envelope. The higher-entropy adiabat in the metallic envelope means higher temperatures and lower densities at pressures of interest. If the dissolution of the heavy elements and the higher-entropy adiabat in the metallic envelope are included in the EOS used in the interior models, the differences between the density profiles might be less significant than shown above. The empirical interior model presented here is preliminary, as the five-degree polynomial density plus constant core density Eq. (9) may be not sufficient to describe the realistic density profile in Jupiter. The polynomial density distribution that has more terms is more capable of describing the density profile in Jupiter, but more measurements are required to determine the polynomial coefficients. More precise gravitational measurements may allow one to achieve the more realistic density profile for Jupiter. In this work, the resulting density profile consistent with the available data is used to calculate the NMOI and k_2, both of which are average physical quantities over the internal density distribution. The comparison to the other NMOI values presented below suggests that there is only a small change with the different density profiles. We expect more realistic treatments for the density profile to have only minor effects on the calculated NMOI and k_2, although changes in the internal density distribution are expected.

Figure 2 shows the calculated NMOI as a function of core mass m_C and core radius x_C, respectively. The allowed two-layer models are constrained by three extreme cases. Case (1) corresponds to the maximum core density of $\rho_C = 30$ g cm^{-3}. In this case, a_C is fixed at a certain value and m_C is varied from zero up to the maximum core mass of 0.12585. The resulting x_C values are varied up to roughly 0.18. Case (2) corresponds to the maximum core mass of $m_C = 0.12585$ where m_C is fixed at the value of 0.12585 and a_C is decreased from the maximum core density of 30 g cm^{-3}. The resulting x_C values are varied from 0.18 to 0.32. Case (3) corresponds to the zero density jump $\Delta\eta_{CEB} = 0$ at the CEB, for which m_C (x_C) is fixed at a certain value and then x_C (m_C) is determined by the condition $\Delta\eta_{CEB} = 0$. For Case (1) the core size increases with increasing the core mass in order to keep the core density unchanged. When the density becomes more centrally condensed, the NMOI shows an obvious decreasing tendency. For Case (3) the core size also increases with increasing the core mass. But the NMOI shows a smooth increasing tendency with increasing core mass or size. This is because the zero density jump requires a decreasing of the core density as the core mass and size both increase. When the core mass is fixed and the core size is increasing, as one would expect, the NMOI increases. This is indeed for Case (2). In addition, if one ignores the shape of the internal density profile and calculates the NMOI with Eq. (15) rather than Eq. (16), the calculated NMOI values are generally decreased by about 3.87%. However, the systematic variations of the

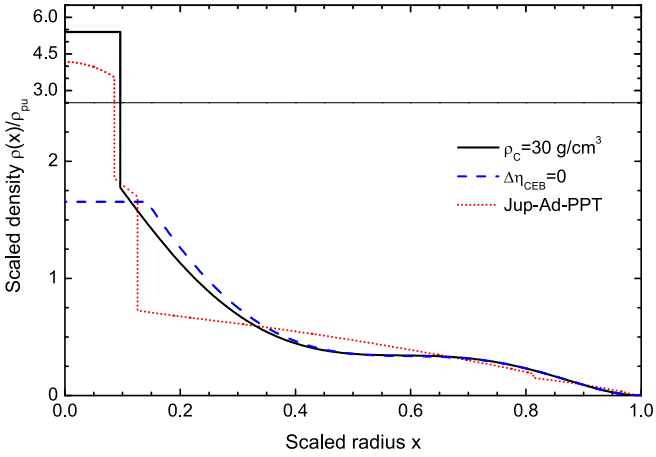

Fig. 1. Density profiles of Jupiter models with the core mass fraction $m_C = 0.020$. Black solid, blue dashed, and red dotted curves correspond to the maximum core density of $\rho_C = 30$ g cm^{-3}, the zero density jump at the CEB $\Delta\eta_{CEB} = 0$, and the three-layer model of Guillot (1999; denoted by Jup-Ad-PPT), respectively. For the sake of clarity, the density values are normalized by a constant density $\rho_{\rm pu} = M/R_p^3 = 5.555$ g cm^{-3} and the upper and lower parts distinguished by thin solid horizontal lines are shown in the different linear scales.

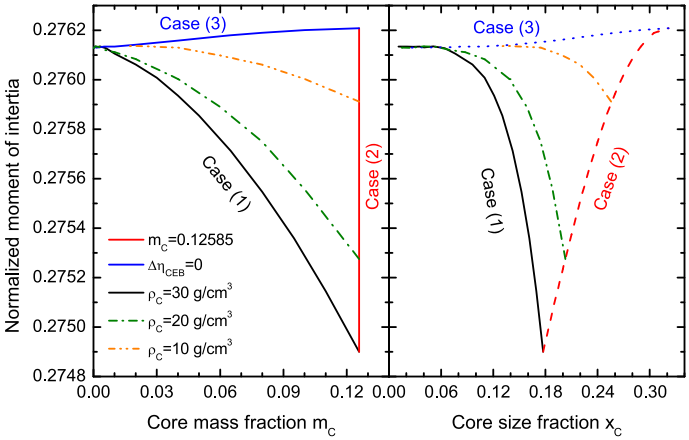

Fig. 2. Jupiter's normalized moment of inertia (NMOI) as a function of core mass fraction (*left*) and core size fraction (*right*). Black solid, red dashed, and blue dotted curves correspond to Case (1), Case (2), and Case (3), respectively (for details of these three extreme cases, see the text). The allowed results are constrained by these three extreme cases. It is suggested that the measured NMOI can be used as a useful constraint to the interior models of Jupiter. Additionally, solutions for core densities of $\rho_C = 20$ and 10 g cm^{-3} are, respectively, shown by green dash-dot and orange dash-dot-dot lines.

Table 2. Jupiter's core properties, equatorial radius, and gravitational harmonic coefficients, compared with the available observed data.

m_C (M_J)	x_C (R_p)	ρ_C (g cm^{-3})	R_e (km)	J_2 $\times 10^6$	J_4 $\times 10^6$	J_6 $\times 10^6$	J_8 $\times 10^6$
	data		71492 ± 4	14696.514 ± 0.272	−586.623 ± 0.363	34.244 ± 0.236	−2.502 ± 0.311
0.100	0.164	30.0[a]	71492.6	14696.513	586.991	32.696	2.807
0.010	0.076	30.0[a]	71492.6	14696.519	586.899	33.047	2.864
0.126[b]	0.200	20.9	71492.6	14696.513	587.012	32.638	2.796
0.126[b]	0.300	6.19	71492.6	14696.511	586.832	33.170	2.883
0.100	0.289	5.49[c]	71492.6	14696.514	586.836	33.295	2.904
0.010	0.108	10.5[c]	71492.6	14696.510	586.891	33.082	2.869

Notes. [(a)]This corresponds to Case (1) with the maximum core density $\rho_C = 30$ g cm^{-3}. [(b)]This corresponds to Case (2) with the maximum core mass $m_C = 0.12585$. [(c)]This corresponds to Case (3) with the zero density jump $\Delta\eta_{CEB} = 0$.

NMOI values with the core properties are almost the same in both cases.

In Fig. 2, the NMOI values range from about 0.2749 to roughly 0.2762 with a variation of 0.5% and they are correlated with the core properties. The NMOI value of about 0.2749 well constrains the core properties, corresponding to the core mass of 40 $M_\oplus$ and the core radius of 0.177 R_p. As the NMOI value becomes larger, the uncertainties of the core properties increase: lighter core masses are allowed and uncertainties of core radii get enhanced. For example, the NMOI value of 0.2755 corresponds to the core mass of 25–40 $M_\oplus$ and the core radius of 0.150–0.225 R_p. When the NMOI values are comparable with 0.27613, the requirement that the core density $\eta_C(x)$ is always larger than $\eta_E(x)$ comes into play and reduces the uncertainties of the core properties. One can see that such large NMOI values correspond to heavier core masses and larger core radii. But the corresponding core density is relatively small, 5–10 g cm^{-3}, suggesting an icy core in Jupiter. Very recently interior models based on ab initio computer simulations have been reused to investigate Jupiter's interior according to the improved determination of Jupiter's gravity field obtained from *Juno* spacecraft (Wahl et al. 2017b). It was demonstrated that dilute cores expanded through a region 0.3–0.5 times Jupiter's radius make the calculated gravitational moments J_n more consistent with the *Juno* gravity measurements. The dilute core means the density jump $\Delta\eta_{CEB}$ at the CEB is small or vanishing. So the dilute-core region just lies below Case (3) in Fig. 2, corresponding to the NMOI values larger than 0.2761. Nettelmann et al. (2012) presented an improved ab initio hydrogen EOS and investigated the internal structure and thermal evolution of Jupiter within the standard three-layer model. The NMOI was then computed from the resulting density profile as $C_N = 0.27605 \pm 0.03\%$. The Hubbard & Militzer (2016) preliminary Jupiter model constructed an axisymmetric interior density profile to fit pre-*Juno* data using the three-dimensional CMS method and the NMOI was calculated as $C_N = 0.27596$. Wahl et al. (2017b) reported on a selection of interior models based on ab initio simulations of hydrogen-helium mixtures where the calculated NMOI values were found to range from 0.27598 to 0.27653. As can be seen, the NMOI values that we calculated above are in reasonable agreement with these results.

It is also of interest to discuss the correlation of the calculated NMOI with core densities besides core masses and radii. As additional information, Fig. 2 also illustrates the NMOI value as functions of the core mass and size fractions for different core densities of respectively $\rho_C = 10$, 20, and 30 g cm^{-3}. As

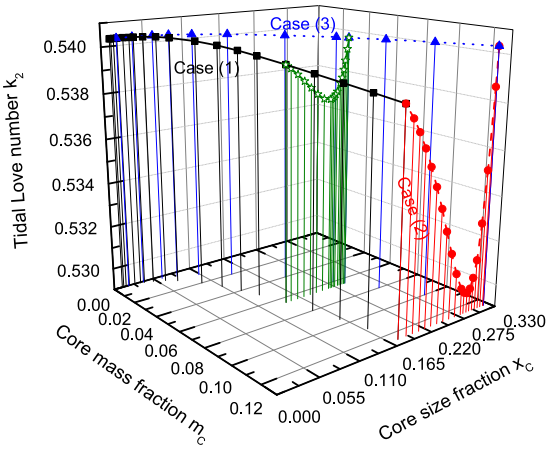

Fig. 3. Calculated tidal Love number k_2 as a function of core mass and size fractions for three extreme cases (for details of these three extreme cases, see the text): the results for Case (1) are denoted by black solid lines with solid squares, the results for Case (2) are denoted by red dashed lines with solid circles, and the results for Case (3) are denoted by blue dotted lines with solid triangles (for details of these three extreme cases, see the text). The solutions for the case with the constant mass fraction $m_C = 0.065$ are also shown by green lines with open stars.

mentioned above, the core size fraction increases with increasing the core mass fraction to keep constant core densities and the calculated NMOI values decrease with increasing the core mass (or size). The larger the core density, the more significant the decreasing behavior. It can also be seen that planets with a denser core can have a smaller NMOI than planets with a sparser core. If the measured NMOI is smaller than 0.2753, with an uncertainty of about 0.2%, it may be used to constrain the core density, suggesting that the core density is not smaller than 10 g cm^{-3}. Although this can tell us no more information about the core components, it serves as a good preliminary probe.

Next, we turn to the tidal Love number k_2. Kramm et al. (2011) investigated the tidal Love number k_2 in simple multi-layer models, where the density distribution internal to a planet is given by analytical expressions and not consistent with the measured gravitational coefficients. The degeneracy of k_2 is found owing to the outer density discontinuities in the three-layer model. Here the two-layer density profile is constrained by the *Juno* gravitational measurements and then employed to evaluate k_2. The variation of k_2 in dependence on the core mass

and size is shown in Fig. 3 for Cases (1–3). Focusing on Case (2), the degeneracy of k_2 over the core size is clearly demonstrated. That is, there is a non-unique relation between the Love number k_2 and the core size fraction x_C. This not only confirms the results of Kramm et al. (2011) but also points out that the degeneracy of k_2 can also emerge in the two-layer model in addition to the three-layer model. It is well known that the tidal Love number k_2 measures the degree of central condensation of a planet's mass: planets with a more inhomogeneous mass distribution can exhibit a smaller Love number k_2 and planets with a central core can exhibit an even smaller Love number k_2. In this work, the density profile in the envelope has to be adjusted to fit Jupiter's gravity field while the core properties are varied. These two aspects affect the Love number. We have employed the envelope density at the CEB combined with the core size as a measurement of the density homogeneity in the envelope. It is described and illustrated in Appendix A for Cases (1–3). In Case (1), the core mass increases with increasing the core size to keep the constant core density, implying the more centrally condensed. And meanwhile the resulting envelope density at the CEB decreases with increasing the core size, implying the more homogeneous mass distribution in the envelope. The core effects take a dominant role in this case. Therefore, it is not so surprising that the k_2 number decreases with increasing the core size. In Case (3) where the density jump is fixed at zero, the core mass increases with increasing the core size but the core density equaling the envelope density at the CEB decreases with increasing the core size. The core effect is not comparable with that in Case (1) and could be counteracted by the envelope effect a certain extent. As a result, there are tiny changes in the calculated k_2 values. In Case (2) where the core mass fraction is fixed at $m_C = 0.12585$, the envelope density at the CEB increases with increasing the core size, implying the more inhomogeneous mass distribution in the envelope. But the density jump at the CEB decreases from about 27.0 g cm^{-3} to zero with increasing the core size. When the density jump is large enough for the denser core to exist, corresponding to the region of the smaller core radii, the envelope becomes more inhomogeneous with increasing the core radius, bringing in a decreasing of the Love number. When the density jump is too small to be observed, corresponding to the region of the larger core radii, the nonexistence of the core results in a considerable increasing of the Love number, as shown in Fig. 3. In order to further illustrate this, the results of the constant core mass fraction $m_C = 0.065$ are also displayed in Fig. 3 and the same behavior is seen as the $m_C = 0.12585$ case. As one would expect in Fig. 3, the well depth of the Love number becomes more shallow as the core mass fraction is decreased.

Despite the degeneracy of k_2 over the core properties, it is still able to tell us information on the central core just like the NMOI. In analogy to Fig. 2, Fig. 4 shows the variation of the Love number k_2 as a function of the core mass m_C and core size x_C, respectively. By projections onto the $k_2 - m_C$ and $k_2 - x_C$ planes, it is noticed that the curves for Cases (1–3) are not sufficient to constrain the two-layer models of Jupiter in contrast to the NMOI. For the case of constant core mass, as shown by the red dashed and green solid lines in Fig. 3, there exits a minimum value of k_2 as a function of the core size fraction x_C. Such minimum values do indeed constitute a new constraint in the $k_2 - m_C$ plane, instead of Case (1). In the $k_2 - x_C$ plane, additional cases are allowed besides the closed region constrained by the curves for Cases (1–3) and hence the partial curves for Cases (1&2) are replaced by the purple dash-dotted curve. As can be seen, the calculated k_2 values range from about 0.5299 to roughly

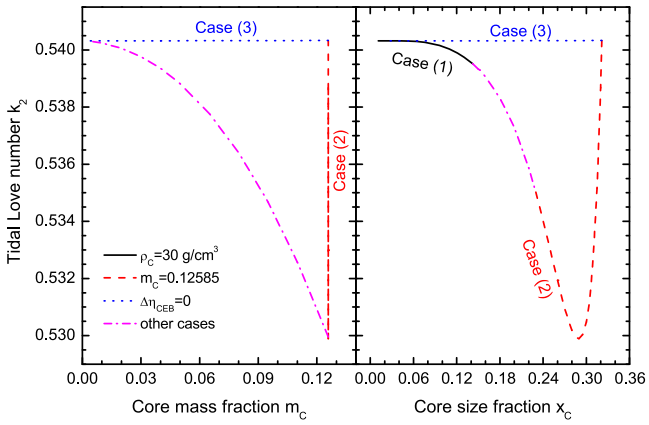

Fig. 4. Jupiter's tidal Love number k_2 as a function of core mass fraction (*left*) and core size fraction (*right*). Black solid, red dashed, and blue dotted curves correspond to Case (1), Case (2), and Case (3), respectively (for details of these three extreme cases, see the text), and purple dash-dotted curves stand for the other cases. The allowed results are constrained by these four curves.

0.5403 with a variation of 1.9%. As usual, the larger k_2 values correspond to larger uncertainties of the core mass and size. For example, the k_2 value of 0.535 corresponds to the core mass of 29–40 $M_\oplus$ and the core radius of 0.23-0.32 R_p. A combination of measurements of Jupiter's NMOI and k_2 can provide better constraints on the core properties of Jupiter. There are other estimations of the static Love number k_2 since the pioneering work of Gavrilov et al. (1975). For example, Gavrilov & Zharkov (1977) constructed Jupiter models fitted to the currently known gravity field J_2 and J_4 and calculated the static tidal response of Jupiter. The Love number k_2 was evaluated as $k_2 = 0.379$, smaller than our k_2 values. Vorontsov et al. (1984) considered a non-rotating giant planet perturbed by a single satellite with an inertial orbital frequency Ω_s in the planet's equatorial plane. A non-rotating model of Jupiter was fitted to the observed J_2 value and a novel approach based on free-oscillation theory was introduced to calculate the tidal response. Taking the limit $\Omega_s \to 0$, Vorontsov et al. (1984) obtained the static tidal response of Jupiter, $k_2 = 0.541$, which is close to our upper limit of k_2. Wahl et al. (2016) introduced the non-perturbative CMS method to calculate the static tidal response of Jupiter, achieving a value of $k_2 = 0.5900$. They also calculated the static tidal response of non-rotating planets using the identical density profile of rotating models and concluded a non-rotating value of $k_2 = 0.53725$. Our calculated k_2 values are in reasonable agreement with this value.

Figure 5 illustrates the correlation of the Love number k_2 with the core density, where the calculated k_2 values are shown as functions of the core mass and size fractions for different core densities of respectively $\rho_C = 10$, 20, and 30 g cm^{-3}. The extreme case of $\Delta\eta_{CEB} = 0$ is also illustrated in the figure, since the results for lower core densities are confined by the requirement $\Delta\eta_{CEB} \geq 0$ especially in the $k_2 - x_C$ plane. As one can seen, the calculated k_2 values decrease with increasing the core mass (or size) like the calculated NMOI. However, in contrast to the NMOI, the larger the core density, the smoother the decreasing behavior. It seems that planets with a sparser core can have a smaller k_2 than planets with a denser core. If the core density is larger than 10 g cm^{-3}, the Love number k_2 should be more than 0.532. In turn, if the measured k_2 is smaller than 0.534 with an uncertainty of about 0.6%, it suggests that the core density is smaller than 20 g cm^{-3}. Combining this with

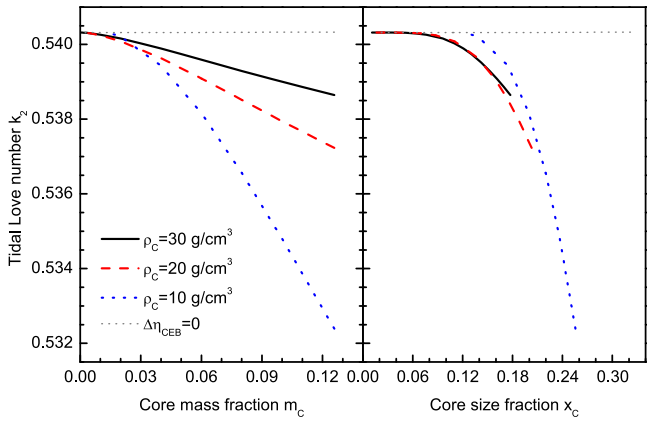

Fig. 5. Jupiter's tidal Love number k_2 as a function of core mass fraction (*left*) and core size fraction (*right*). The curves show solutions for core densities of ρ_C = 30 (black solid lines), 20 (red dashed lines), and 10 (blue dotted lines) g cm^{-3}, respectively. The extreme case of $\Delta\eta_{CEB} = 0$ is also illustrated by thin gray dotted lines.

the NMOI analysis, one can further constrain the core density of Jupiter.

4. Summary

We have presented in this paper an empirical two-layer model to deduce possible density profiles in Jupiter, generalized from the works of Anderson & Schubert (2007); Helled et al. (2009). Different two-layer models can be constructed in terms of core properties, and then radial density profiles in Jupiter are constrained by *Juno*'s gravity field observations. In addition to gravitational harmonic coefficients, both moments of inertia and tidal Love numbers are sensitive to the internal density distribution of a planet. So they are potentially observational constraints by the *Juno* mission to further constrain the interior models of Jupiter. In order to discern their abilities to constrain the interior models, their dependence on the core mass and size is investigated.

The calculated NMOI values are varied from 0.2749 to 0.2762 with a variation of 0.5%. This variation is attributed to varied core properties. By illustrating the NMOI values of various two-layer interior models as shown in Fig. 2, we achieve several acceptable models for a given NMOI value, although the NMOI values are degenerate in portions of the parameter space. A subset of the NMOI range $C_N < 0.2756$ would only be obtainable for the interior models with larger core mass and higher core density, where the core size fraction is distributed around $x_C = 0.177$ and its uncertainty increases with increasing the NMOI value. The calculated tidal Love number k_2 is varied from 0.5299 to 0.5403 with a variation of 1.9%. In contrast to the NMOI, the non-unique correspondence between the k_2 value and the core size is found for the two-layer models with constant core mass. This is consistent with the conclusion of Kramm et al. (2011), where the degeneracy of k_2 over the envelope density discontinuity was found within the three-layer model. By illustrating the k_2 values of various two-layer interior models as shown in Figs. 4 and 5, measurements of k_2 can still help constraining Jupiter's two-layer interior models. A subset of the k_2 range $k_2 < 0.536$ would only be obtainable for the interior models with larger core mass, larger core size, and lower core density. However, if larger values of the NMOI or Love number k_2 are measured, a highly degenerate area can be seen where they appear to be less able to distinguish the interior models with small cores regardless of the core density.

A combination of measurements of the NMOI and Love number k_2 could reduce the uncertainties of the core mass and size. For instance, the NMOI value of $C_N = 0.2756$ exhibits the core of $m_C = 0.075 - 0.126$ and $x_C = 0.149 - 0.227$ and the Love number of $k_2 = 0.536$ exhibits the core of $m_C = 0.083 - 0.126$ and $x_C = 0.217 - 0.316$. The combination of them yields the core of $m_C = 0.083 - 0.126$ and $x_C = 0.217 - 0.227$, where the significant reduction of the core size uncertainty is seen. Moreover, the combination of the NMOI and k_2 measurements could also limit the core density because they exhibit the opposite behavior as the core density is varied. For instance, the NMOI range of $C_N \leq 0.2759$ implies the core density of $\rho_C \geq 10$ g cm^{-3} and the k_2 range of $k_2 \leq 0.537$ implies the core density of $\rho_C \leq 20$ g cm^{-3}. The resulting core density is hence limited as 10 g cm^{-3} $\leq \rho_C \leq$ 20 g cm^{-3}.

The present analysis is merely preliminary because the actual situation of Jupiter's interior is more complex than what we consider here. The data available on Jupiter's shape and gravity field may be not sufficient to deduce the realistic density profile in Jupiter. The internal density profile presented here has the lower density at intermediate depths and the higher density at deeper depths with respect to the three-layer model of Guillot (1999), as shown in Fig. 1. The differences between the internal density profiles should have influence on both the calculated NMOI and k_2 values. However, the existing comparison to the other NMOI values suggests that there is only a small shift. This is because both the NMOI and k_2 are average physical quantities over the internal density distribution in which the shifts in the values may counteract with each other. One should be careful with estimates about the core properties derived from NMOI and k_2 as degeneracy may occurs, and additional observational constraints are needed to narrow the uncertainty about the core properties. Besides, more precise estimation of gravitational coefficients and tidal Love numbers could be worth in future modeling efforts. The CMS method is a good option in evaluating the self-consistent shape and gravity field of rotating liquid planets (Hubbard 2013; Hubbard & Militzer 2016) as well as the static tidal response from a satellite Wahl et al. (2016, 2017a). Besides, Kong et al. (2016) investigated the effect of the zonal winds on the gravity field of Jupiter in a fully self-consistent multi-layered model. They found that the effect is weak with a variation of less than 1% for J_2, J_4, J_6 but becomes substantial for the high-order coefficients $J_{n\geq 10}$. Kaspi et al. (2016) calculated the gravitational harmonics resulting from internal dynamics using different methods: the thermal wind approach and the two independent barotropic models including the potential theory method of Hubbard (1999) and CMS method of Hubbard (2013). So the interior modeling effort will be assisted by including dynamical contributions.

Acknowledgements. We thank G. Schubert and K. Zhang for valuable discussions. This work is supported by the Science and Technology Development Fund of Macau under Grants No. 278/2017/A, No. 007/2016/A1, and No. 119/2017/A3.

References

Anderson, J. D, & Schubert, G. 2007, Science, 317, 1384
Becker, A., Lorenzen, W., Fortney, J., & Nettelmann, N. 2014, ApJS, 215, 21
Bolton, S. J., Adriani, A., Adumitroaie, V., et al. 2017, Science, 356, 821
Folkner, W. M., Iess, L., Anderson, J. D., et al. 2017, Geophys. Res. Lett., 44, 4694
Fortney, J. J., & Nettelmann, N. 2010, Space Sci. Rev., 152, 423

Gavrilov, S. V., & Zharkov, V. N. 1977, Icarus, 32, 443
Gavrilov, S. V., Zharkov, V. N., & Leontev, V. V. 1975, Astron. Zh., 52, 1021
Guillot, T. 1999, Planet. Space Sci., 47, 1183
Guillot, T. 2005, Annu. Rev. Earth Planet. Sci., 33, 493
Helled, R. 2012, ApJ, 748, L16
Helled, R., Anderson, J. D., Schubert, G., & Stevenson, D. J. 2011, Icarus, 216, 440
Helled, R., Schubert, G., & Anderson, J. D. 2009, Icarus, 199, 368
Hubbard, W. B. 1999, Icarus, 137, 357
Hubbard, W. B. 2013, ApJ, 768, 43
Hubbard, W. B., & Militzer, B. 2016, ApJ, 820, 80
Kaspi, Y., Hubbard, W. B., Showman, A. P., & Flierl, G. R. 2010, Geophys. Res. Lett., 37, L01204
Kaspi, Y., Davighi, J. E., Galanti, E., & Hubbard, W. B. 2016, Icarus, 276, 170
Kong, D., Zhang, K., & Schubert, G. 2016, ApJ, 826, 127
Kramm, U., Nettelmann, N., Redmer, R., & Stevenson, D. J. 2011, A&A, 528, A18
Kramm, U., Nettelmann, N., Fortney, J. J., Neuhäuser, R., & Redmer, R. 2012, A&A, 538, A146
Lainey, V., Jacobson, R. A., Tajeddine, R., et al. 2017, Icarus, 281, 286
McMahon, J. M., Morales, M. A., Pierleoni, C., & Ceperley, D. M. 2012, Rev. Mod. Phys., 84, 1607
Miguel, Y., Guillot, T., & Fayon, L. 2016, A&A, 596, A114
Militzer, B., & Hubbard, W. B. 2013, ApJ, 774, 148
Militzer, B., Hubbard, W. B., Vorberger, J., Tamblyn, I., & Bonev, S. A. 2008, ApJ, 688, L45
Militzer, B., Soubiran, F., Wahl, S. M., & Hubbard, W. 2016, J. Geophys. Res. Planets, 121, 1552
Nettelmann, N., Holst, B., Kietzmann, A., French, M., & Redmer, R. 2008, ApJ, 683, 1217
Nettelmann, N., Becker, A., Holst, B., & Redmer, R. 2012, ApJ, 750, 52
Saumon, D., & Guillot, T. 2004, ApJ, 609, 1170
Saumon, D., Chabrier, G., & van Horn, H. M. 1995, ApJS, 99, 713
Seidelmann, P., Kenneth, P., Archinal, B. A., et al. 2007, Celest. Mech. Dyn. Astr., 98, 155
Vorontsov, S. V., Gavrilov, S. V., Zharkov, V. N., & Leontev, V. V. 1984, Astron. Vestn., 18, 8
Wahl, S. M., Hubbard, W. B., & Militzer, B. 2016, ApJ, 831, 14
Wahl, S. M., Hubbard, W. B., & Militzer, B. 2017a, Icarus, 282, 183
Wahl, S. M., Hubbard, W. B., Militzer, B., et al. 2017b, Geophys. Res. Lett., 44, 4649
Zharkov, V. N., & Trubitsyn, V. P. 1975, Astron. Zh., 52, 599
Zharkov, V. N., & Trubitsyn, V. P. 1978, Physics of Planetary Interiors (Tuscon: Pachart Pub. House)

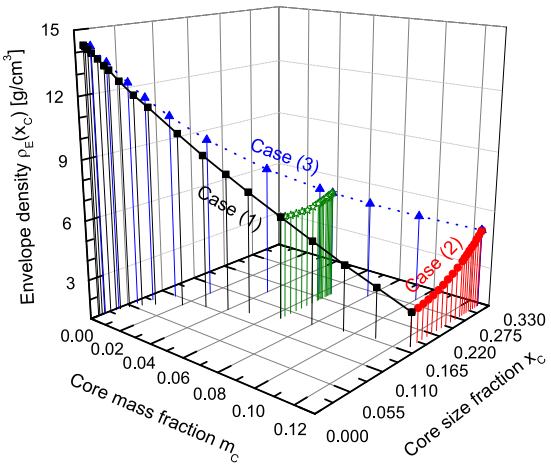

Fig. A.1. Same as in Fig. 3, but for the envelope density at the core-envelope boundary (CEB) $x = x_C$.

Appendix A: Envelope density at the core-envelope boundary (CEB)

In this work, the density profile in the envelope had to be adjusted to fit Jupiter's gravitational field while the core properties are varied. With this in mind, besides the core effect on the static tidal Love number k_2, the variation of the envelope density profile also affects the Love number k_2. In order to understand the latter effect, Fig. A.1 shows the envelope density at the CEB as a function of the core properties for Cases (1–3) (for details of these three extreme cases, see the text). This quantity combined with the core size can be regarded as a measurement of the density homogeneity in the envelope. In general, the larger the envelope density at the CEB, the more inhomogeneous the envelope in mass distribution, implying a smaller Love number k_2.